

# CHARACTERIZATION OF SOLID PARTICLE CANDIDATES FOR APPLICATION IN THERMAL ENERGY STORAGE AND CONCENTRATING SOLAR POWER SYSTEMS

Patrick Davenport<sup>1,a)</sup>, Zhiwen Ma<sup>1,b)</sup>, Jason Schirck<sup>2</sup>, William Nation<sup>2</sup>,  
Aaron Morris<sup>2</sup>, Xingchao Wang<sup>1,3</sup>, Matthew Lambert<sup>4</sup>

<sup>1</sup> National Renewable Energy Laboratory, 15013 Denver W Pkwy, Golden, CO 80401, USA.

<sup>2</sup> School of Mechanical Engineering, Purdue University, West Lafayette, IN 47907, USA.

<sup>3</sup> Colorado School of Mines, 1500 Illinois St, Golden, CO 80401, USA.

<sup>4</sup> Allied Mineral Products, 2700 Scioto Parkway, Columbus, OH 43221, USA.

a) Corresponding author: [PDavenport@PraecisED.com](mailto:PDavenport@PraecisED.com)

b) Corresponding author: [Zhiwen.Ma@nrel.gov](mailto:Zhiwen.Ma@nrel.gov)

## Abstract

Thermal energy storage (TES) enables concentrating solar power to remain competitive in the renewable energy mix by firming up intermittent solar resource and providing grid services such as load shifting. Free from siting constraints, stand-alone TES systems show promise as a low-cost alternative to traditional pumped-storage hydropower or compressed air energy storage. At the core of all TES technologies is a storage medium, the selection of which governs many aspects of system design and operation. Although the majority of commercial installations utilize molten salts, solid particles can demonstrate stability over wider temperature ranges. This amounts to increased energy storage densities and corresponding reductions in system cost which is essential in achieving low-cost energy storage. In this work, eight solid particle candidates are systematically identified and screened for application in a specific particle-TES system. The five most promising candidates (CARBO CP and HSP, calcined flint clay (CFC), brown fused alumina (BFA), and silica sand) are further characterized by size and morphology for fluidization suitability, flowability for particle transport, and thermal stability. Calcined flint clay and brown fused alumina are eventually down-selected due to thermal instability at the target operational temperature of 1200°C. Although the physical characteristics of CARBO outperform silica sand in all categories examined, the marginal performance gains are considered insufficient to justify the additional media cost so silica sand is selected as the leading candidate. Within the silica sand ( $\alpha$ -quartz) space, the high end of Geldart Group B particles is identified to satisfy the target fluidization regime for the application of interest without compromising particle flowability. In focused testing, Silica 460 is shown to exhibit sufficient stability through long-duration (500-hour) thermal and cyclic testing (1200°C), 10-hour testing at 1400°C, and in contact with candidate refractory containment materials. Finally, an average heat capacity of 1.1 J/g·°C is measured over 300-1200°C with a quartz inversion enthalpy ( $\Delta H_{\alpha-\beta}$ ) of 10.7 J/g.

## 1. Introduction

Advances in grid-scale, long duration energy storage are necessary to support continued deployment of renewable energies. Traditional pumped-storage hydropower (PSH) is limited by geography, and compressed air energy storage (CAES) is constrained by existing geologic sites. Demonstrated by commercial concentrating solar power (CSP) plants, thermal energy storage (TES) shows promise as a low-cost alternative that is free from siting constraints if operated as a stand-alone system [1].

At the core of all TES technologies is a storage medium, the selection of which governs many aspects of system design and operation. Most state-of-the-art commercial systems utilize molten nitrate salts with operational temperature ranges limited to  $\Delta T < 375^\circ\text{C}$ : freezing below  $\sim 220^\circ\text{C}$  and decomposing above  $\sim 595^\circ\text{C}$  [2]. While these liquid systems are burdened by the need for expensive corrosion-resistant alloys and salt costs ranging from  $\$800$ - $1000/\text{ton}$ , they benefit from relatively mature fluid transport technologies. Other TES mediums including latent-heat phase change materials (PCMs), concrete blocks, and rock or earthen beds can suffer from challenges of limited service temperatures, high cost, poor thermal responsiveness, or instability under cycling.

As an alternative, some solid particles demonstrate stability over temperature ranges in excess of  $1000^\circ\text{C}$ . This stability enhances TES system performance in two ways, each of which are essential in achieving low-cost electric energy storage: (1) it results in an increase in sensible energy storage density and corresponding decrease in required volumes of both media and containment; and (2) it supports more efficient power cycles. Nonetheless, particle-based systems face their own challenges: fixed or moving-packed bed designs are often limited by low heat transfer rates, and moving-packed or fluidized bed designs are disadvantaged by a comparatively less mature industry for transport of hot solids which can be accompanied by attrition/abrasion.

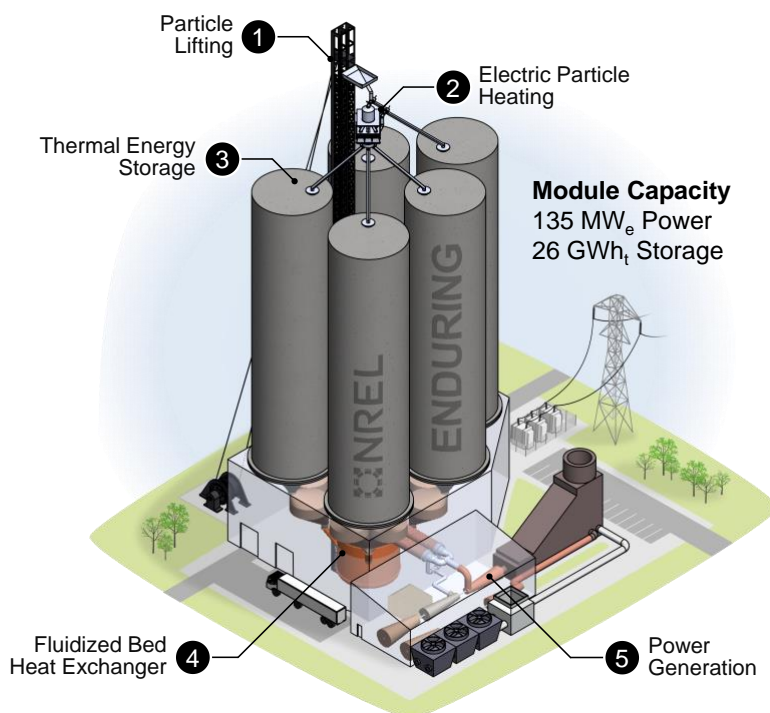


Figure 1. Artist's rendition of a stand-alone particle-TES system under development at NREL [3,4].

Figure 1 shows a solid particle and gas, two-phase flow TES system under development at the U.S. Department of Energy’s (DOE) National Renewable Energy Laboratory [5–7]. The stand-alone system charges by heating solid particles using off-peak, low-price electricity before storing the particles for 10-100 hours in highly-effective insulated hot silos [8]. During peak hours, the storage system discharges by gravity feeding the hot particles through a fluidized bed heat exchanger to transfer the particle heat to a power cycle for electrical generation (e.g., conventional steam-Rankine, air Brayton turbine with combined-cycle ability, or emerging sCO<sub>2</sub> Brayton power cycle).

Considerable particle research has been conducted for CSP efforts that value media with a high solar-weighted absorptivity for direct-absorption particle receiver designs [9]. However, in the case of the stand-alone TES system, particle selection is no longer governed by radiative properties, but instead, by particle thermal and mechanical stability, flowability, fluidization quality, and cost which is sensitive to bulk density, heat capacity, and media abundance. Operating under this new paradigm, the authors were motivated to reevaluate solid particle candidates to find that which is most suitable to support the stand-alone system shown in Figure 1. The selected particle is critical as it governs many aspects of the system and component design and operation: for more details on the system, component design, and estimated costs, readers are encouraged to refer to [5–8].

Figure 2 outlines the particle selection approach used in this work. At a high level, eight particle candidates are screened for suitability as a particle-TES media. The five most promising candidates are further characterized by size and morphology for fluidization suitability, flowability for particle transport, and thermal stability. Results reveal silica sand, in the form of  $\alpha$ -quartz, to be the most suitable candidate for the particle-TES system of interest. Finally, Silica 460 is subject to several resource-intensive tests to investigate stability over long-duration and thermal cycling, measure specific heat capacity, and test for containment compatibility.

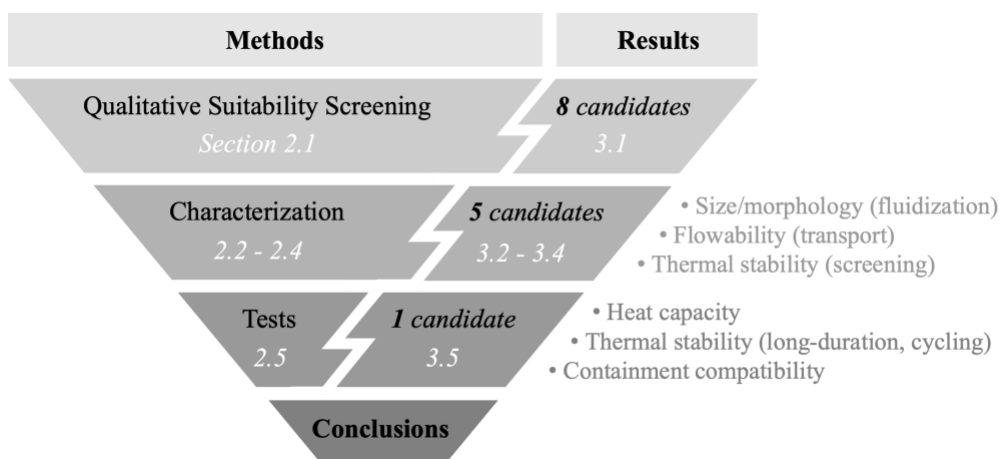


Figure 2. Iterative particle selection approach utilized in this work.

## 2. Supporting Materials and Methods

### 2.1. Qualitative Suitability Screening

To focus characterization efforts on the most promising particles, a multi-step screening process was conducted. The process includes: (1) identifying desirable particle attributes and assigning weights; (2) determining an initial particle candidate pool (aided by literature review); and (3) screening the initial pool by a weighted comparison of the desirable particle attributes. The initial candidate pool is presented in this section to aid the reader by prefacing promising candidates. The pool is reduced further through the screening process, and only particles which pass are subject to more resource-intensive, experimental characterization methods.

Table 1 summarizes the desirable attributes, considerations, influential metrics, and general targets for the stand-alone particle- TES system. Top candidates should demonstrate high thermal stability, a suitable combination of low particle cost and high thermal capacitance, good flowability and fluidization quality, and high mechanical stability. For each attribute, the authors assigned a weight ranging from one to five, where five is considered of critical importance for the application. The last three attributes are assigned lower weights at this screening stage because they are more challenging to assess by literature alone. Highlighted text indicates the metrics that are investigated experimentally following the screening.

Table 1. Desirable particle attributes and weights for the stand-alone system.

Desirable Attribute	Considerations	Influential Metrics	Target	Assigned Weight
High Thermal Stability	- Increased storage density - Improved flowability	- Melt temperature / softening char. - Containment compatibility	> 800°C (sCO <sub>2</sub> /Brayton)	4
Low Cost	- Reflects abundance of particles - Incorporates embodied energy	- Naturally sourced - Synthetic / engineered	< 3\$/kWh [10]	5
High Thermal Capacitance	- Increased storage density - Reduced storage volume	- Apparent (bulk) / real densities - Heat capacity	< 3\$/kWh [10]	3
Good Flowability	- Facilitate solids handling - Avoid ratholing* - Avoid particle segregation	- Particle size & morphology - Flow function coefficient - Effective angle of internal friction	$\phi_p > 150\mu\text{m}$	3
Fluidization Quality	- Target fluidization regime - Effective heat transfer	- Particle class, size, & morphology - two-phase HTF flow rate	$\phi_p < 700\mu\text{m}$	2
High Mech. Stability	- Low attrition rate - Low particle refreshing rate - Improved service life	- Polymorphic phase changes - Thermal expansion & hardness - Attrition and system abrasion rates	> 10-year active life	2

Notes: Highlighted text indicates metrics that are investigated experimentally in this work following screening.

\* The formation of a narrow vertical flow channel during solids discharge which can cause stagnation in the surrounding region, uneven discharge, and enhanced particle segregation.

A review of particle- TES literature with emphasis on cost and thermal stability was conducted to survey the landscape for candidates that may support the stand-alone particle- TES system. In particular, the authors used the following chronologically-ordered works to justify eight initial particle candidates: O. Ercan Ataer describes various general principles of TES with a section dedicated to thermophysical properties of different solid storage media [11]; Siegel et al. evaluate optical properties of commercially available proppants for use in CSP- TES applications [12];

Baumann and Zunft characterize the thermophysical, thermomechanical, tribological and rheological of select particles [13]; Baeyens et al. report on thermophysical, thermomechanical, and attrition behavior of select particles the European Union's Next-CSP effort [14]; Diago et al. characterize UAE desert sands to assess the suitability for use as TES media [15]; Kang et al. assess the suitability of various particle-types for CSP-TES [16]; and Schroeder and Albrecht investigate the effect of thermal cycling on particle candidates [17].

Figure 3 shows the eight initial particle types arranged in order of increasing cost, together with approximate thermal stability limits and mineral compositions. Note that cost was retrieved from a combination of public sources and vendor discussion, and varies depending on market demand and desired particle size. Broader thermal stability ranges generally reflect candidates with either amorphous or variable solid solution compositions that can exhibit softening transitions rather than distinct melting points. To conclude the process, this pool of candidates is screened by the weighted comparison of desirable particle attributes.

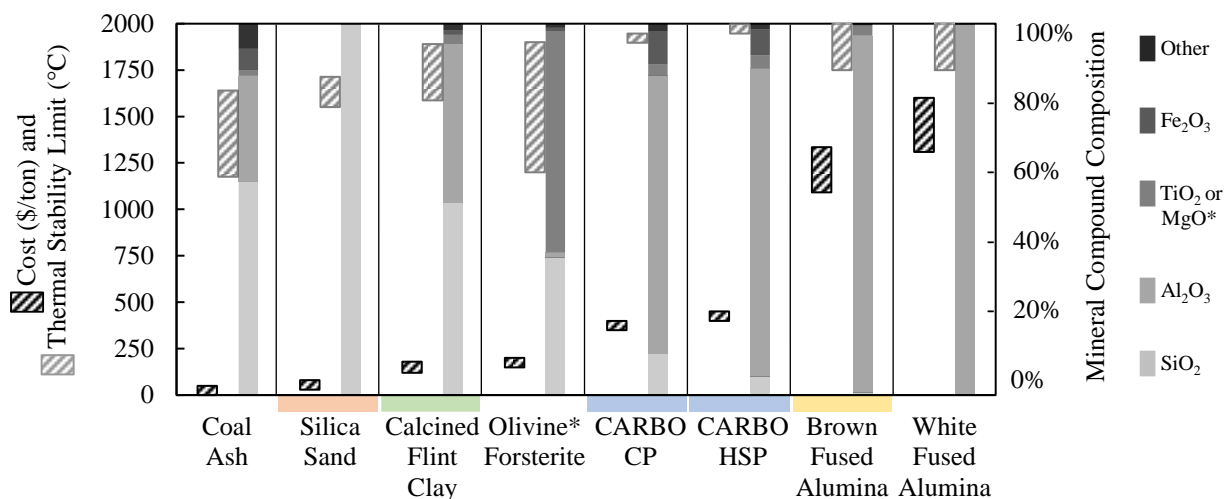


Figure 3. Approximate cost, thermal stability limit, and mineral compound composition of eight initial TES particle candidates. The four colors used here for silica sand, calcined flint clay (CFC), CARBO, and brown fused alumina (BFA) will be maintained throughout this work. \* The mid-gray tone for Mineral Compounds represents TiO<sub>2</sub> for all particles except Olivine Forsterite, where it represents MgO.

## 2.2. Size and Morphology Fluidization Suitability

Particle size, density, and morphology influence critical aspects of particle transport and the fluidized bed heat exchanger design including flowability and fluidization type and quality, system superficial gas velocity, and achievable heat transfer coefficients.

Figure 4 shows a diagram of Geldart particle groups where each groups' fluidization characteristics are governed by density and particle size: *Group C* exhibits cohesiveness (flours); *Group A* is largely aeratable (fine powders); *Group B* (granular) particles show bubble formation at or slightly above minimum fluidization; and *Group D* (coarse) particles allow gas to bypass in a mode different from *Group A* or *Group B* particles, often resulting in poor solids mixing despite turbulent gas flow and potential for increased attrition [18].

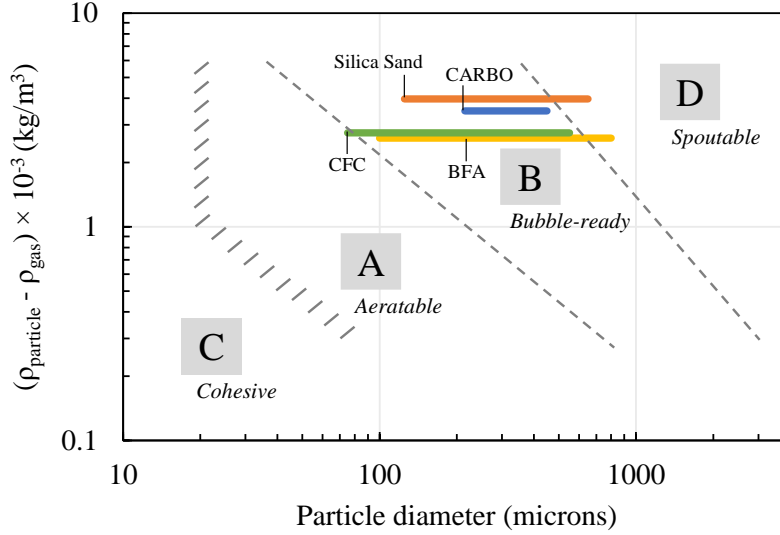


Figure 4. Diagram of Geldart particle classification groups with the five promising particle candidates' distributions marked by horizontal solid lines. Note that both CARBO distributions, CP and HSP, are included in the one line.

To help evaluate the suitability of each particle candidate, particle size distributions were characterized by Mie scattering using a Malvern Mastersizer 3000. A refractive index of 1.457 (silica) was used for silica sand and calcined flint clay; 1.766 (alumina) for brown fused alumina; and 1.120 (bauxite) for both CARBO proppants. A particle sampling probe was used to separate subsamples from the bulk sources and mitigate the influence of particle segregation during transport. The five most promising particle candidates are marked in Figure 4 by horizontal solid lines whose ranges span the approximate particle distributions obtained from vendors (note that both of the CARBO product distributions are included in the one line, similar to the other candidates' respective overlapping distributions).

Particle morphology was characterized using a Malvern Morphologi G3-ID. Values are reported in a volume distribution transformation, wherein, individual instances are scaled relative to particle size. Figures of interest include circularity, high-sensitivity (HS) circularity, aspect ratio, solidarity, and convexity, each of which is defined here:

Circularity (Eq. (1)) is the ratio of the circumference of a circle equal to the particle's projected area to the perimeter of the particle which can range from 0 to 1 (i.e., a perfect circle). When comparing particles of similar circularity, it can be useful to square the figure resulting in a more sensitivity measure sometimes referred as high-sensitivity (HS) circularity or compactness.

$$\text{Circularity} = \frac{2 \cdot \sqrt{\pi \cdot A}}{\text{Perimeter}} \quad \text{HS Circularity} = \frac{4\pi \cdot A}{\text{Perimeter}^2} \quad (1)$$

Aspect ratio (Eq. (2)) is the ratio of particle width to length which can range from 0 to 1.

$$\text{Aspect Ratio} = \frac{\text{width}}{\text{length}} \quad (2)$$

Solidarity (Eq. (3)) is the ratio of the particle area to the area enclosed by the convex hull. The convex hull can be seen as the profile created by an imaginary elastic band wrapped around the particle and in-plane with the image.

$$\text{Solidarity} = \frac{A}{A+B} \quad (3)$$

Convexity (Eq. (4)) is the ratio of the perimeter of the convex hull to the particle which can range from 0 for more irregular, rough and spiky particles to 1 for more smooth particles.

$$\text{Convexity} = \frac{\text{Perimeter of } A+B}{\text{Perimeter of } A} \quad (4)$$

### 2.3. Flowability for Particle Transport

Good particle flowability is important for the stand-alone system for two main reasons: it permits the use of shallower design angles in hoppers and transport pipes, which in turn, reduces the system's required particle lift height, cost, as well as system attrition rates.

Particle flowability was primarily characterized according to the *Standard Shear Test Method for Bulk Solids* (ASTM 6673-02) using a Schulze RST-XS ring shear cell tester. This method determines the flow function and wall friction angles which can be used to calculate hopper angles required to achieve mass flow conditions. The tests were run at ambient temperature with a major consolidating pressure of 5 kPa. A brief description of the test process is included here and aided by Figure 5 (left):

1. The test begins with application of a maximum preload normal stress. The shear stress is then increased until steady-state shear flow is observed, and both cell loads are removed.
  2. After applying a reduced normal stress, shear stress is applied again until a maximum shear stress is collected, marked by a point of "incipient flow".
  3. The preload normal stress is then reapplied to the system and the shear stress is increased to reach preload conditions.
- Separated by preload conditions, steps 2 and 3 are repeated at other normal stresses.

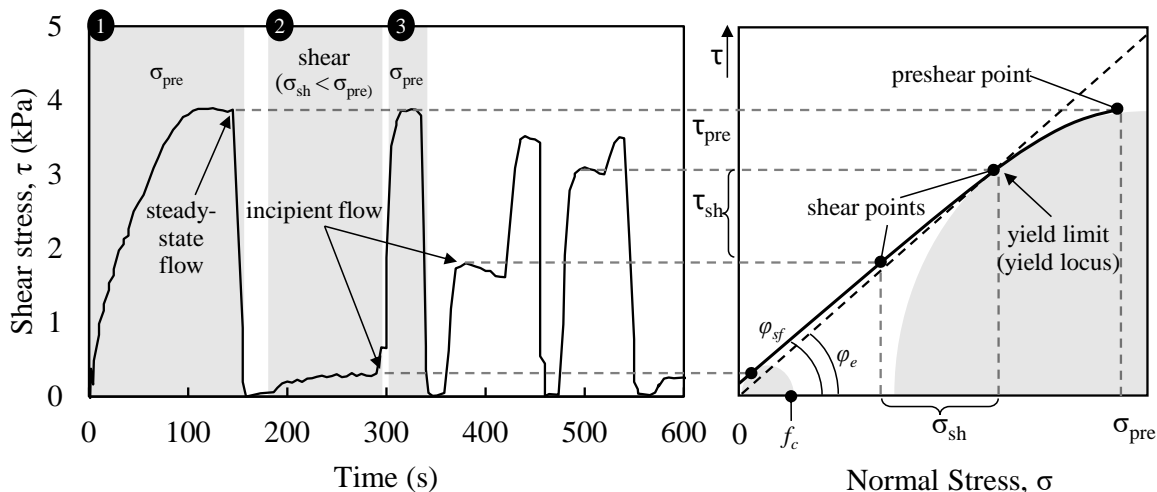


Figure 5. Example of data processing for the ring shear cell tester including acquired shear stress profiles (left) and extraction of meaningful particle flow attributes (right).

Figure 5 (right) shows the plotting of three shear test points and a best fit function drawn through the points forming a yield locus. The origin and shear points define two Mohr's circles that correspond to the unconfined yield strength ( $f_c$ ) and the major principal (consolidation) stress ( $\sigma_1$ , not shown as it extends beyond the plot).

The ring shear cell test reveals various particle flow attributes. The flow function (flowability) coefficient ( $ff_c$ ) is determined as the ratio between the major principal stress ( $\sigma_1$ ) and the unconfined yield strength, where  $\sigma_1$  is specified by the user and  $f_c$  is determined from measurement. High flowability coefficients indicate good flowability, while lower indicate bulk cohesiveness. The angle of internal friction at steady-state flow ( $\varphi_{sf}$ ) is measured between the line that intersects the yield locus and tangent to the circle corresponding with the unconfined yield strength, and the normal stress axis. Similarly, the effective angle of internal friction ( $\varphi_e$ ) is measured between the line that intersects tangent to the major principal stress circle and the origin, and the normal stress axis. With careful application, the shear cell test also reveals the apparent (bulk) density ( $\rho_b$ ). The real density ( $\rho$ ) was measured using an AccuPyc Helium pycnometer, presented in this work as the average of 7-10 measurements. These attributes all help characterize bulk flowability and reveal important information required for proper design of bulk-handling containers/devices.

## 2.4. Thermal Stability Screening

Exceptional particle thermal stability is required for the stand-alone system of interest. Inadequate thermal stability can manifest in either inter-particle agglomeration or intra-particle attrition. Inter-particle agglomeration or adhesion/deposition on surfaces complicates system operation by hindering particle flow, inducing particle segregation, and/or shifting fluidization characteristics away from the design point. Intra-particle attrition caused by thermal shock or cycling fatigue can have a similar effect on segregation and fluidization, but also reduces useful particle life, requiring eventual media replenishment. Alkali metals, even at small concentrations, should be avoided as the low first ionization energy promotes lower melting temperatures—a physical phenomenon leveraged by fluxing agents to induce ceramic sintering at lower temperatures.

Thermal stability limits were investigated by heating particles to successively higher temperatures in a Lindberg/Blue M™ box furnace. The samples were prepared in 5ml alumina crucibles as shown in Figure 6, then heated with a ramp rate of 10°C/min to either 800, 1000, or 1200°C, held for 10 hours, then left to cool at the natural cooling rate of the furnace which does not exceed the heating rate. An additional candidate, SEMCOA (calcinated mullite), was sourced in crude form (i.e., relatively broad particle distribution) and included in this test only.

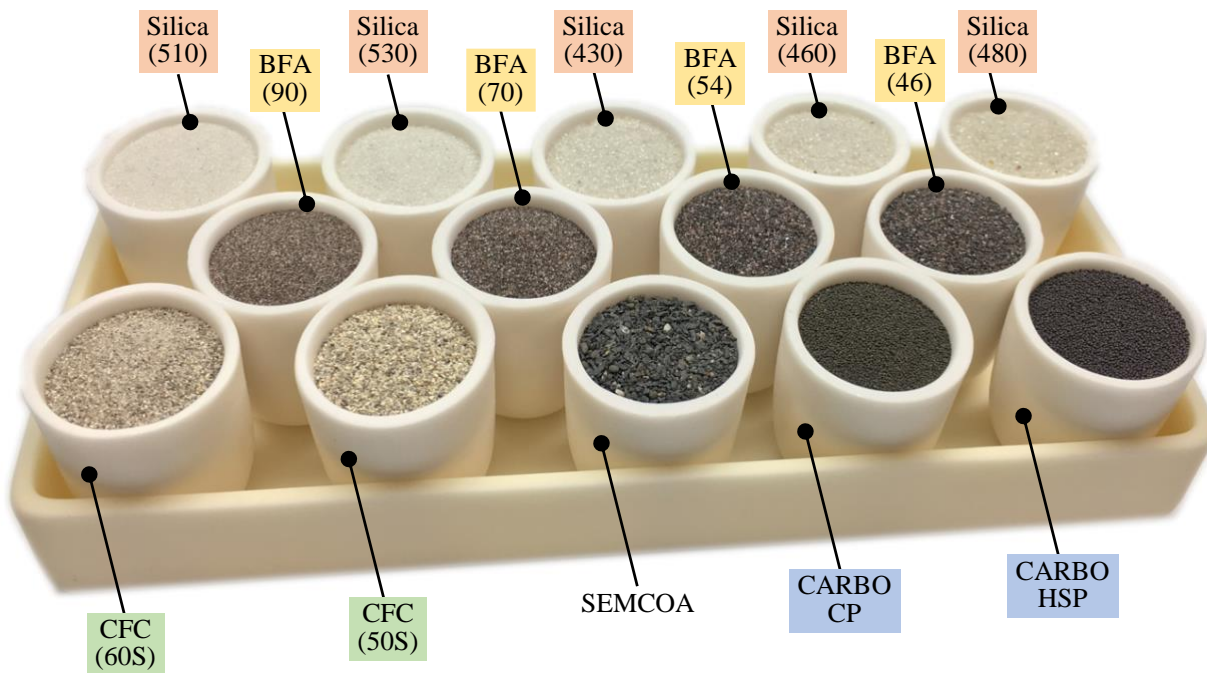


Figure 6. Particles and distributions subject to thermal stability testing.

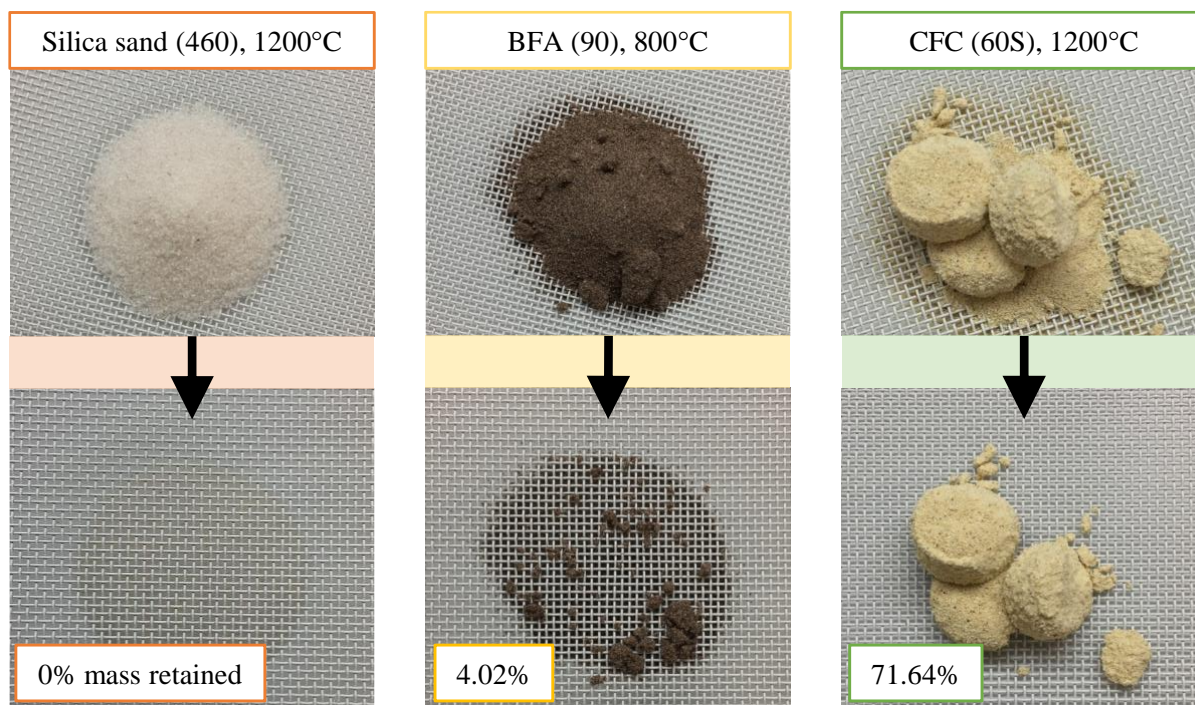


Figure 7. Examples of testing method for soft/hard particle agglomeration.

The authors are unaware of a standard to evaluate soft agglomeration of particles, so a practical method was devised: (1) after each thermal treatment, a Tyler 16-mesh (1mm openings) was placed on top of each crucible followed immediately by a thin piece of hardboard; (2) the mesh/hardboard and crucible were gently turned upside-down; (3) the crucible is lifted allowing the particles to pile with some angle of repose; (4) the mesh is lifted to rest on standoffs, separating it from the hardboard by approximately 2cm to allow non-agglomerated particles to fall through; (5) the weight of particles remaining on the mesh (if any) is measured and compared to the initial amount. Exemplary photos of the method and mass retained are shown in Figure 7.

## **2.5. Focused Tests: Heat Capacity, Thermal Endurance and Cycling, and Containment Compatibility**

The leading particle candidate is subject to four additional, resource-intensive tests. The tests include: (1) measurement of particle specific heat capacity; (2) stability over long-duration, thermal cycling, a dwell in excess of the design point temperature; (3) containment compatibility testing which continues to challenge similar liquid phase TES efforts; and (4) a containment compatibility test under compressive load.

Particle heat capacity is determined by differential scanning calorimetry (DSC), taking the average of four sweeps from 1200 to 300°C. Enthalpy of the alpha-beta quartz inversion is determined by integrating between the experimental data and two piecewise, linear functions fit to the alpha and beta data in the proximity of the phase change.

For long-duration stability, particles are heated with a ramp rate of 10°C/min to 1200°C and held for 500 hours. This test is conducted three times, each under a different atmosphere relative to varied potential power turbine configurations: air, humidified air (pH<sub>2</sub>O=50%), and nitrogen. A volumetric furnace refresh rate of ~15-minutes is maintained. For thermal cycling, particles are cycled at a ramp rate of 5°C/min between 300°C and 1,200°C with a 1-hour dwell period at both extremes. Samples were removed and analyzed after 25, 50, and 100 cycles. For both thermal tests, particle distributions pre- and post-treatment are characterized by Mie scattering as described in Section 2.2. For the 500-hour treatment in air, pre- and post-treatment powder x-ray diffraction is conducted at 1°/min on Silica 460 using a Rigaku DMax. An additional 10-hour dwell at 1400°C is conducted to test particle stability under potential electric resistive heating conditions which would exceed the storage temperature (1200°C).

For containment compatibility, nine candidate hot-face refractory samples are partially submersed in Silica 460 particles during all three long-duration, 500-hour stability tests. The candidate hot-face refractories were supplied by Allied Mineral Products and include INSULMIX® 80LIP, PETROMAX® 700 LT, and INSULCAST® 280 AL, each fired at either 110°C, 315°C, or 650°C. CARBO is also tested in contact with the three 110°C refractories. Data collected includes the mass gain/loss for each insulation sample as well as general observations (e.g., discoloration and removal difficulty after test). To gain insight into durability, the same set of insulation samples were used for all three tests.

Lastly, a containment compatibility test was conducted under a compressive load. First, a crucible was cast from each of the three insulation materials and fired at 1200°C. The crucibles were then partially filled with silica sand, and a ~140 kPa compressive load was created using high alumina

rods cast into 16.5 lb blocks, as shown in Figure 8. The assemblies were heated at 2.3°C/min to 1200°C and held for 100 hours.



Figure 8. Compatibility testing with silica particles in crucible under a 140 kPa compressive load, which is similar in magnitude to that expected during operation [5].

### 3. Results and Discussion

#### 3.1. Qualitative Suitability Screening

Table 2 shows the weighted comparison of desirable particle attributes and scores for each of the initial candidates. In general, thermal stability, cost, and thermal capacitance are evaluated quantitatively by comparing relevant values from literature; flowability and fluidization by observing particle morphology and available particle size distributions with focus on distribution breadth and median particle diameter; and mechanical stability by mineral hardness, tenacity, and fracture. In this work, high hardness is considered a favorable particle attribute: however, other applications may choose to reevaluate the tradeoffs between particle and system wear. The top five candidates selected to pass screening are CARBO HSP, CARBO CP, silica sand, brown fused alumina, and calcined flint clay, while white fused alumina, olivine, and coal ash do not. The following sections share other key considerations for each of the initial eight candidates.

Table 2. Suitability screening by a weighted comparison of desirable particle attributes.

Media Candidate	Thermal Stability	Low Cost	Thermal Capacitance	Good Flowability	Fluidization Quality	Mechanical Stability	Overall Score
<b>Weight</b>	<b>4</b>	<b>5</b>	<b>3</b>	<b>3</b>	<b>2</b>	<b>2</b>	(weight × score)
Coal Ash	1	5	2	2	2	2	49 ×
Silica Sand	2	5	3	4	5	4	✓ 72
Calcined Flint Clay	3	4	3	3	3	3	✓ 62
Olivine (Forsterite)	3	4	3	2	2	4	59 ×
CARBO CP	4	1	4	5	3	5	✓ 64
CARBO HSP	4	1	4	5	3	5	✓ 64
Brown Fused Alum.	5	2	5	2	2	4	✓ 63
White Fused Alum.	5	1	5	2	2	4	58 ×

**Coal ash** is appealing because, as a byproduct of power plants, cost can approach 0\$/ton [19]. Among the two main forms, *bottom ash* from combustion furnaces is generally too coarse to meet desired fluidization criteria, but fly ash collected from particulate control devices (electrostatic precipitators or baghouses) may be suitable for some TES applications even though the majority of particles fall below the 150 μm target from Table 1. Depending on the coal source and combustion practices, chemical compositions of fly ash will vary from Figure 3 which reflects ash collected from Ohio’s J.M. Stuart Generating Station [20]. For fly ash (and also all other particle candidates) a presence of alkali metals should be avoided as combustion research shows it can lead to lower temperature necking and eventual agglomeration of fluidized bed particles which could have dire consequences for both fluidization and flowability [21–23]. Together, the fine particle distribution, potential for alkali content, and lower thermal stability limits are likely to result in cohesion during transport and agglomeration during fluidization.

**Silica sand** particles in the ultra-pure form of α-quartz (>99%) ranging from 20-2000 μm in diameter are available in abundance across the U.S. Midwest. Despite the purity, the particles often appear golden yellow due to thin coatings of iron oxides and/or hydroxides [24]. Quartz is among the most stable of naturally occurring minerals and is resistant to most chemical attacking

solutions. The mineral is aided further by a high hardness and lack of preferred cleavage, which helps the silica sand particles resist other agents of weathering like mechanical attrition. High-purity silica sand is the most common fluidized bed media due to high fusion temperatures, naturally round morphology, and low cost due to limited processing steps (~\$30-80/ton). When heated, low-temperature  $\alpha$ -quartz undergoes a rapid and reversible, displacive transformation at 573°C to high temperature  $\beta$ -quartz. Due to the displacive (and not reconstructive), nature of the transformation, this *quartz inversion* is thought to have limited impact on particle stability for monocrystalline particles. Moreover, the release of crystallographic stress likely contributes to the high melting temperature of  $\beta$ -quartz (1713°C). For more information, please refer to the author's focused evaluation of silica sand for use as TES media [25].

**Calcined flint clay** (CFC) is the product of high temperature calcination (>450°C) of naturally occurring kaolin, a hydrated aluminosilicate [26]. The result is the evolution of water and the formation of new compounds that generally exhibit refractory properties and adequate thermal shock resistance, though the additional processing step adds to overall cost (~\$180/ton). Since the  $\text{Al}_2\text{O}_3/\text{SiO}_2$  fractions of natural kaolin sources and the calcination temperature can vary, an array of calcined flint clays and properties exist which can increase system design complexity. Similarly, the amorphous nature results in a softening glass transition temperature rather than a distinct melting point.

**Olivine** is an abundant, magnesium iron silicate mineral group that can exist as a solid solution with any fraction of magnesium/iron  $(\text{Mg,Fe})_2\text{SiO}_4$ , where the thermophysical properties transition rather smoothly between pure forsterite ( $\text{Mg}_2\text{SiO}_4$ ) and fayalite ( $\text{Fe}_2\text{SiO}_4$ ). With a higher melting temperature of ~1890°C [27], forsterite-rich sources are preferred over fayalite (1205°C) for thermal energy storage applications. While pure forsterite quarries do not exist, large sources of dunite (92% forsterite, 8% fayalite) and peridotite (88% forsterite, 12% fayalite) are available [24]. Additionally, forsterite can be synthesized between 1100-1400°C by solid-state reactions of MgO and  $\text{SiO}_2$ , though synthetic sources have exhibited agglomeration at temperatures at and below 1000°C, likely due to the presence of amorphous silica [28]. Other suitable characteristics include the absence of a well-developed cleavage characteristic (similar to silica sand), and a relatively high real density (3400 kg/m<sup>3</sup>) and heat capacity (1.25 kJ/kg·K) [16].

**CARBO** (CP / HSP) is a synthetic aluminosilicate used in the oil industry as a fracking proppant, which has also gained traction in CSP as a direct solar absorbing material candidate due to its high solar absorptivity, thermal stability, and the exceptional roundness achieved by spray-drying. Although the media cost far exceeds naturally occurring options and solar absorptivity is not relevant to the stand-alone particle-TES of interest, CARBO characteristics can be used to help benchmark other candidates since it has been examined in many studies.

**Fused alumina** is synthesized by fusing raw bauxite ore (~\$100/ton) in an arc furnace before crushing and milling the product to the desired final distribution. High purity processing (>99%  $\text{Al}_2\text{O}_3$ ) yields white fused alumina, while lower purities (<95%) are sold as brown fused alumina (BFA), both of which exhibit high strength and chemical resistance (both acid/alkali). Although  $\text{TiO}_2$  is incorporated in the fusion process to strengthen the material, due to its hardness, BFA may demonstrate sensitivity to attrition and thermal shock. In today's market, TBC mesh sizes 46-54 (330-411  $\mu\text{m}$ ) are most economical, but the price is still likely to exceed \$1,000/ton due to the costly synthesis process. For the same reason, BFA can garner on the order of \$220/ton in recovery potential, though material transport may offset the recovery benefit.

### 3.2. Size and Morphology Fluidization Suitability

The box plots in Figure 9 show commercially-available particle distributions characterized for the five candidates. Diameter data is reported in D[4,3] form (i.e., as the *volume-weighted* or *mass moment* mean). Continuous distributions of the same data sets indicate that all candidates are monodisperse in nature. *Group B* Geldart ranges are identified using the difference in density of particle masses and air under design point conditions.

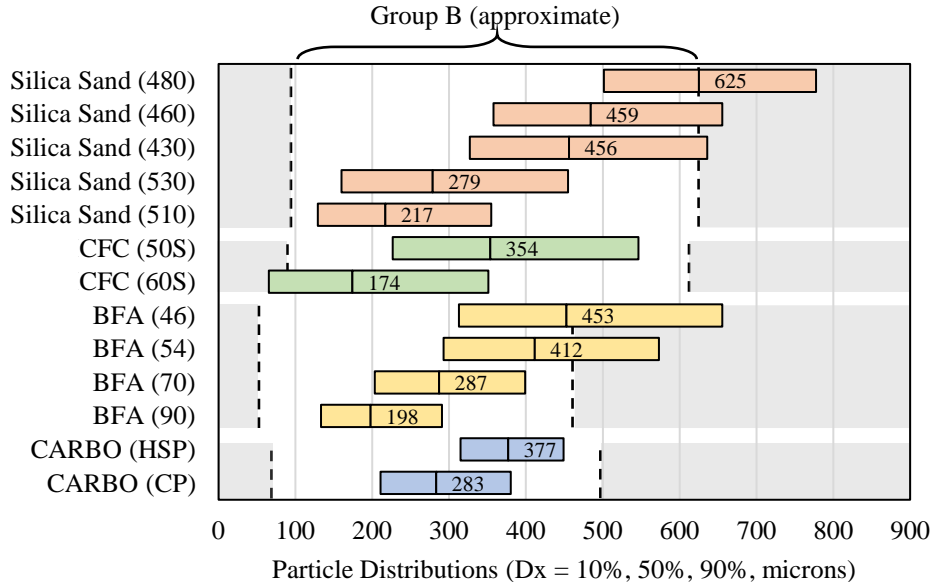


Figure 9. Particle distributions and median diameters obtained via Mie scattering. *Group B* Geldart ranges are identified using the difference in density of particle masses and air under design point conditions [18].

Figure 10 shows a diagram of fluidization regimes as a function of dimensionless particle diameter ( $d_p^*$ ) and dimensionless superficial gas velocity ( $U^*$ ) with the Geldart particle groups identified [18]. It serves as a map for fluidization conditions: as gas flow rate is increased, the bed passes through minimum fluidization ( $U_{mf}^*$ ) and can eventually transition into turbulent fluidization or even exceed the terminal velocity of the particle ( $U_t^*$ ). For *Group A* and *B* particles, a minimum bubbling threshold ( $U_{mb}^*$ ) and critical bubbling/slugging threshold ( $U_c^*$ ) is identified at which point the bubbles/slugs reach the maximum diameter. Larger superficial velocities lead to bubbles breaking up with pressure fluctuation.

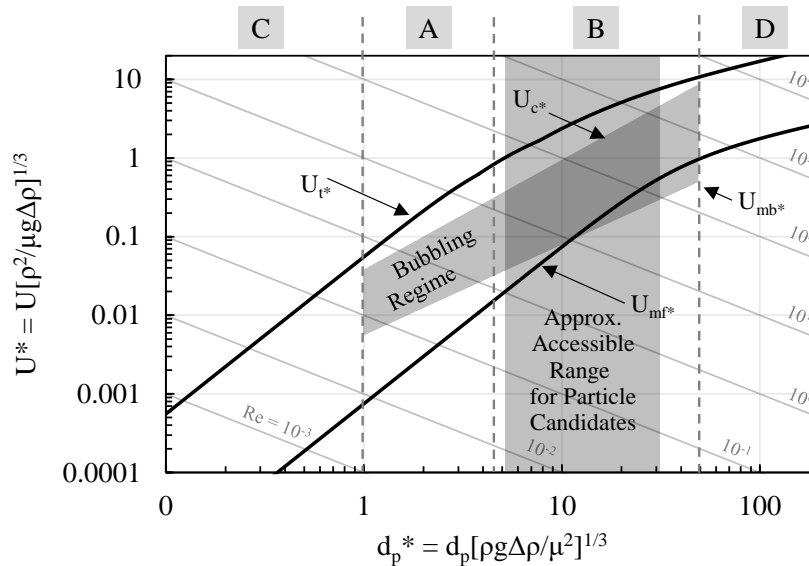


Figure 10. Diagram of general fluidization regimes as a function of dimensionless particle diameter ( $d_p^*$ ) and dimensionless superficial air velocity ( $U^*$ ) with Geldart particle classification. Selected particle candidate distributions fall within the Group B.

For the stand-alone application shown in Figure 1, *Group B* particles are ideal from a particle handling perspective as they maintain a lower minimum fluidization velocity while reduced inter-particle forces which generally leads to good flowability. *Group A* particles are known to demonstrate enhanced heat transfer characteristics which is also appealing. However, care must be taken to ensure that fines do not invoke cohesive nature. Cohesiveness is generally influenced by inter-particulate forces including van der Waals, capillary, electrostatic and magnetic forces depending on particle type. As seen in Figure 9, and highlighted in Figure 10, the particle candidates and varied distributions sourced from vendors fall in the desired *Group B*.

Figure 11 shows results from the Malvern Morphologi G3-ID characterization which include high sensitivity (HS) circularity, aspect ratio, solidarity, convexity, and circularity, accompanied by four exemplary photos to help convey candidate morphologies. The implications of circularity on particle flowability are similar to that of particle sphericity: highly spherical particles are less resistant to flow which can allow systems to maintain mass flow (a first in, first out regime) with shallower hopper angles and reduced facility headroom. Evidenced by higher circularity, silica sand and CARBO products are expected to exhibit better flowability relative to sharper CFC and BFA candidates. The aspect ratios and solidarity values of the CARBO products indicate superior morphology relative to all other candidates. Convexity is a measure of how “spiky” a particle is. The implications of convexity differ from circularity/sphericity in that a circle (sphere) and square (cube) each have a convexity of 1 but markedly different circularities (sphericities). No particularly distinct trends are observed across candidate convexities.

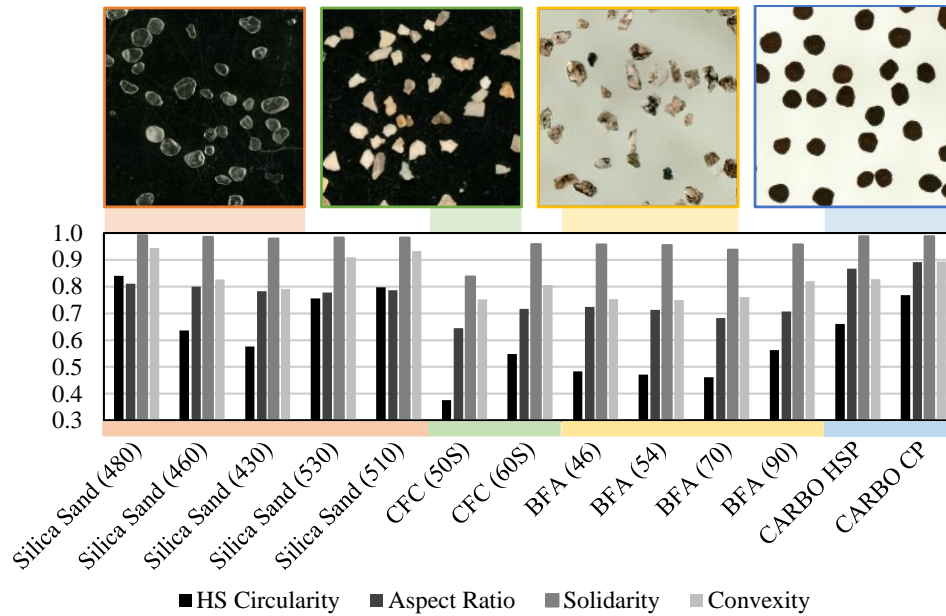


Figure 11. Malvern Morphologi G3-ID characterization results and exemplary photos.

### 3.3. Flowability for Particle Transport

Figure 12 shows results from the Schulze RST-XS shear cell characterization and AccuPyc Helium pycnometer which include real density ( $\rho$ ), bulk density ( $\rho_b$ ), solids fraction, effective angle of internal friction ( $\phi_e$ ), and angle of internal friction at steady-state flow ( $\phi_{sf}$ ).

BFA is shown to have the highest real density (3.96-3.97  $\text{g}/\text{cm}^3$ ), followed by CARBO products, then silica sand and CFC which show a marginal difference. However, BFA and CFC suffer from solid fractions on the order of 10% lower than CARBO and silica sand which is thought to be the effect of the irregular shape and overall reduced circularity/roundness preventing these particles from consolidating more densely. CARBO products have the lowest internal friction angles at steady-state flow and effective friction angles which indicates better bulk flowability.

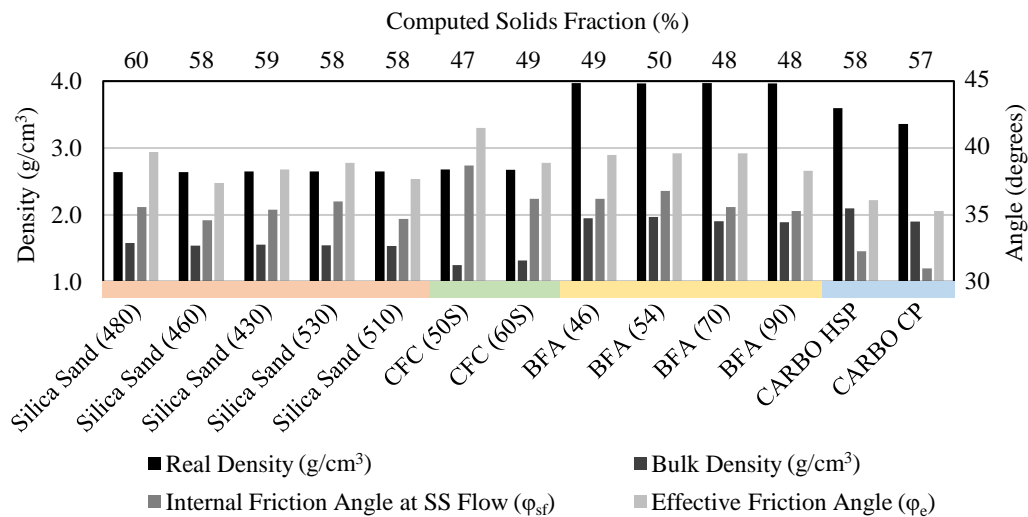


Figure 12. Schulze RST-XS shear cell test results.

Although not shown in Figure 12, all particle candidates demonstrate flowability coefficients ( $ff_c$ ) in excess of 10 which is indicative of “free-flowing” materials according to Jenike & Johanson [29]. This is confirmed by the relatively small difference for all candidates between the effective friction angle ( $\phi_e$ ) and internal friction angle at steady-state flow ( $\phi_{sf}$ ) which is characteristic of easy flowing bulk solids. For reference, flowability coefficients from 4-10 indicate easy-flowing, and coefficients from 2-4 indicate a more cohesive nature.

Testing at ambient temperature may help identify particles whose flowability is poor due to morphology which are also likely demonstrate poor flowability at design point temperature: however, good performance at ambient does not ensure good performance at high temperature, especially if particle (or contaminant) softening occurs at the elevated temperature. Accordingly, future focused work should include testing at design point temperatures.

### 3.4. Thermal Stability Screening

Figure 13 shows results from the thermal stability screening tests as a function of median particle diameter, furnace hold temperature, and percent of mass retained on the mesh indicated by bubble size. Callouts are included to help convey bubble magnitudes and the smallest bubble size represents data points with 0% retained. Evident at all three hold temperatures is the trend of increased soft agglomeration for finer particle samples which may be due to a larger contribution of inter-particle surface forces (e.g., cohesion by Van der Waals) relative to particle mass.

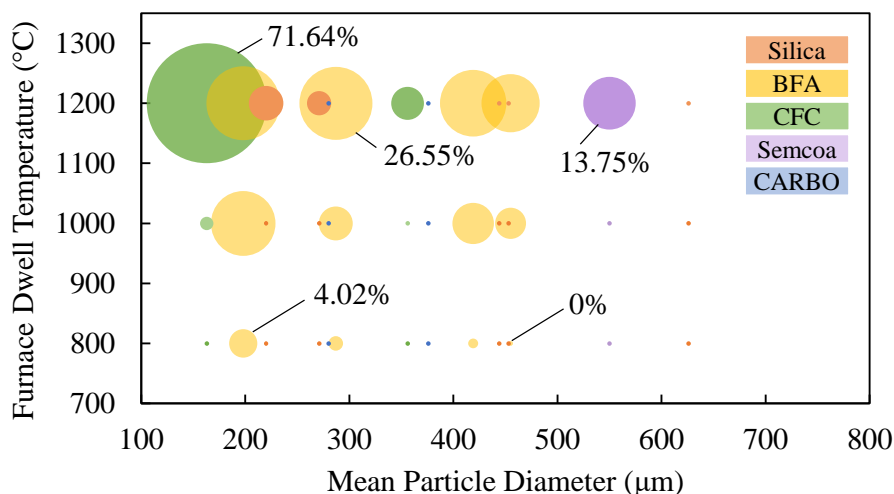


Figure 13. Thermal stability screening results as a function of median particle diameter. Bubble size shows mass retained on a Tyler 16-mesh (1mm openings) following 10 hours at the indicated furnace holding temperature. The smallest bubble size represents data points where 0% mass was retained.

Across all tested sizes, silica sand shows limited tendency for agglomeration at 800 and 1000°C, with soft agglomeration occurring at 1200°C and only for particle distributions with median diameters below 279 µm. Note that this soft agglomeration broke down and passed through the mesh when it was subject to gentle “tapping”. Despite a high melting point, brown fused alumina (BFA) shows soft agglomeration at lower temperatures than all other candidates with increasing severity for smaller particles. This is thought to be due to the increased inter-particle forces that exist between planar contacting surfaces of the relatively sharp/planar particles. Due to the presence of 20-45% amorphous (glassy) silica, both calcined flint clay and SEMCOA demonstrate

harder agglomeration above 1000°C. This is to be expected for compounds containing amorphous silica. CARBO performed the best through this screening test, exhibiting only slight soft agglomeration that broke down during gentle tapping of the mesh.

Although optical characteristics of particles impact the stand-alone system to a limited extent, they can reveal changes in chemical compounds. Figure 14 shows crucibles from select particle candidate distributions where each quarter of the crucible reflects a different thermal condition (i.e., as-received, after 10 hours at 800, 1000, and 1200°C). For all samples, color changes between as-received and 800°C are likely due to removal of hydrates and changes between 800 and 1000°C are thought to be caused by burn-off of organic contaminants. For CARBO products (particularly CP), the change between 1000 and 1200°C is thought to reflect a higher oxidation state. Although silica sand ( $\alpha$ -quartz) undergoes an instantaneous, displacive phase change to  $\beta$ -quartz at approximately 573°C, it recovers at a similar temperature upon cooling, so is unlikely to influence appearance at ambient temperature [25].

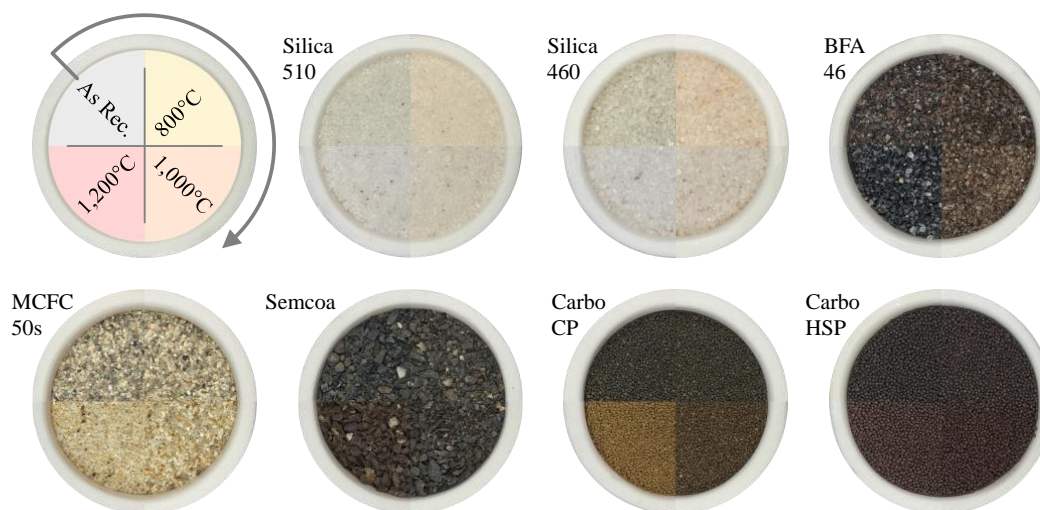


Figure 14. Qualitative color change results of select particles following thermal treatments (ramp to indicated temperature, hold for 10 hours, natural cooling to room temperature).

### 3.5. Focused Tests: Heat Capacity, Thermal Endurance and Cycling, and Containment Compatibility

Findings from all four tests focused tests are presented here for the Silica 460 particle candidate: (1) measurement of specific heat capacity; (2) stability over long-duration, thermal cycling, a temperature dwell in excess of the design point; (3) containment compatibility testing; and (4) containment compatibility under compressive load. Item two consists of a summary as a more detailed account is available in the author's accompanying evaluation of silica sand for TES [25].

Figure 15 shows the average heat capacity for silica sand over four DSC sweeps. The average heat capacity over the 300-1200°C region of interest is approximately 1.1 J/g·°C, which represents a 6.5% decrease relative to NIST measurements, as presented by Chase et al. [30]. The authors consider this reasonable since the thermophysical properties will vary depending on material source. Additionally, the magnitude of quartz inversion can differ depending on the origin and size fraction of the sample, where large particles are shown to favor the  $\alpha$ -phase, while small particles can stabilize the  $\beta$ -phase [31].

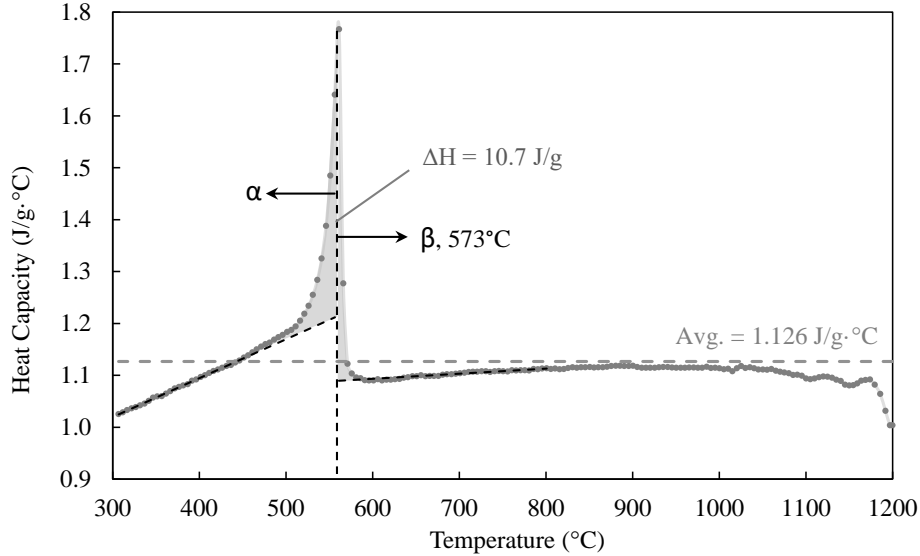


Figure 15. Silica sand heat capacity determined by DSC. An average heat capacity of 1.1 J/g·°C is observed over the 300-1200°C region of interest.

The enthalpy of the alpha-beta quartz inversion ( $\Delta H_{\alpha-\beta}$ ) is determined to be approximately ~10.7 J/g. This agrees with transformation enthalpies tabulated by Ghiorso et al., which range from 80-290 cal/mol (5.57-20.19 J/g), along with their own results obtained from DSC runs over a 9.0°C interval [32]. The volumetric change associated with the transformation is reported at 1.6% [33], which can induce “ratcheting” containment failures if heating repeatedly in a vessel under stationary conditions.

Long-duration and thermal cycling test results for Silica 460 are summarized in Table 3. For long-duration testing, the observed change in median particle diameter by volume ( $D_{v50}$ ) under air, nitrogen, and humidified air is -2.46%, -1.38%, and -2.61%, respectively. For air and humidified air, although the sample count is sufficient to determine statistical significance at the 95% confidence level (unpaired student’s T-test), the cause of the shift could come from other artifacts like particle-segregation in transport, which is notoriously difficult to control. Following the 10-hour dwell at 1400°C, only soft agglomeration was observed (though not quantified as in Figure 13).

Table 3. Summary of long-duration and thermal cycling tests for Silica 460.

Test Type	Temp. (°C)	Duration (hours)	No. of Cycles	Furnace Atmosphere	Relative $\Delta$ ( $D_{v50}$ , %)	Sample Count	Statistically Significant*
Dwell	1200	500	1	air	-2.46	13	Yes
				N <sub>2</sub>	-1.38	15	No
				humidified air (p <sub>H2O</sub> =50%)	-2.61	15	Yes
Cycling	300 - 1200	1	25	air	2.16	3	-
			50		-1.18	3	-
			100		2.86	3	-

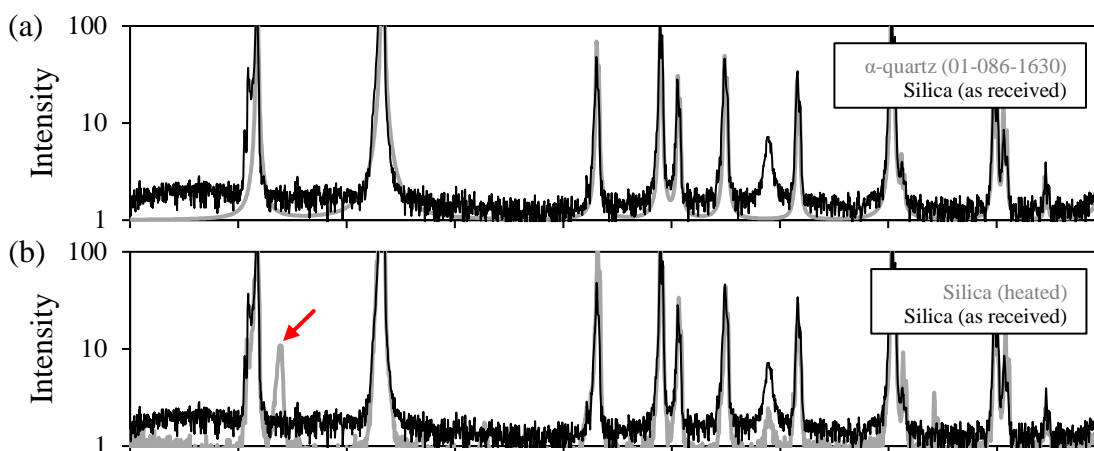
Notes: Duration reflects dwell time at temperature extreme(s) and does not include ramping.

\* Determined via an unpaired student’s T-test when sample count permits.

For the Silica 460 cycling tests, the mean particle diameter is seen to fluctuate which suggests that the observed changes may result from analysis variability, too few samples, sampling process, or artifacts from sample handling or measurement. For example, a burn-out cycle was not performed to clean organic materials or hydrates from the “as received” particle surfaces before establishing a baseline, and these surface contaminants may influence the particle refractive/absorptive indices which are used as input for Mie scattering. Qualitatively, neither test showed signs of agglomeration or sintering upon removal from the furnace.

The cycling results appear more promising than those witnessed by the German Aerospace Center (DLR), where cleavage of similarly sized quartz particles is evidenced after 5, 10, and 30 cycles [13]. However, the mono- vs. polycrystalline nature of particles at DLR was undisclosed, and the cycling process involved water quenching from 810°C, where a cooling rate of 3034°C/s is achieved. This is allegedly ~54% of the theoretical maximum rate (5646°C/s), that the residual tensile stress at the surface of a flawless quartz particle of that size can withstand. The current study may differ in that the particles are confirmed monocrystalline, and that the cooling rate is orders of magnitude lower, leaving a greater margin to accommodate stress concentrations that occur across non-spherical particles and at surface defects. Nonetheless, future cycling efforts should target system design point charge/discharge rates.

Figure 16 compares Silica 460 XRD spectra before and after the 500-hour test in air. By comparing to a theoretical  $\alpha$ -quartz powder diffraction file (PDF), Figure 16 (a) confirms that the *as received* sample is composed of high-purity  $\alpha$ -quartz. Following the heat treatment, Figure 16 (b) shows peak development at  $2\theta = 21.94^\circ$ . By comparing to a theoretical  $\alpha$ -cristobalite PDF, Figure 16 (c) confirms that the peak development at  $2\theta = 21.94^\circ$ ,  $28.37^\circ$ , and  $31.35^\circ$  correspond to  $\alpha$ -cristobalite spacing of the 101, 111, and 102 crystallographic planes, respectively. Quantitative spectral analysis confirms this development with the following shifts in composition:  $\alpha$ -quartz (64.8→47.0%),  $\beta$ -quartz (18.1→30.3%),  $\alpha$ -cristobalite (9.7→17.1%), and tridymite (7.4→5.6%). It should be noted that spectral analysis is highly subjective, depending on consistent sample preparation, machine operation, and additional decisions made by the analyzer. Due to this and the relatively fast scan rate (1°/min), values presented here should only be used to inform broad, relative changes in composition.



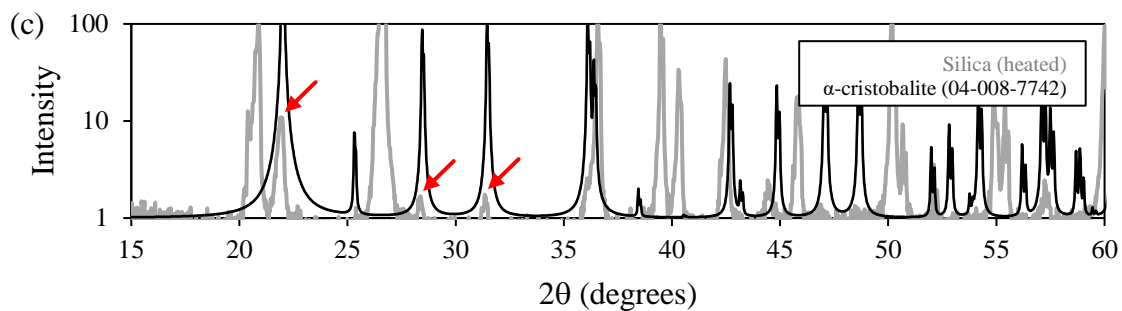


Figure 16. (a) XRD spectra of *as received* and theoretically calculated  $\alpha$ -quartz PDF (01-086-1630) confirm high-purity  $\alpha$ -quartz composition; (b) overlay of *as received* and *heated* spectra show peak development at a  $2\theta = 21.94^\circ$ ,  $28.37^\circ$ , and  $31.35^\circ$ ; (c) overlay of *heated* spectra and theoretically calculated  $\alpha$ -cristobalite PDF (04-008-7742) indicates some degree of cristobalite presence.

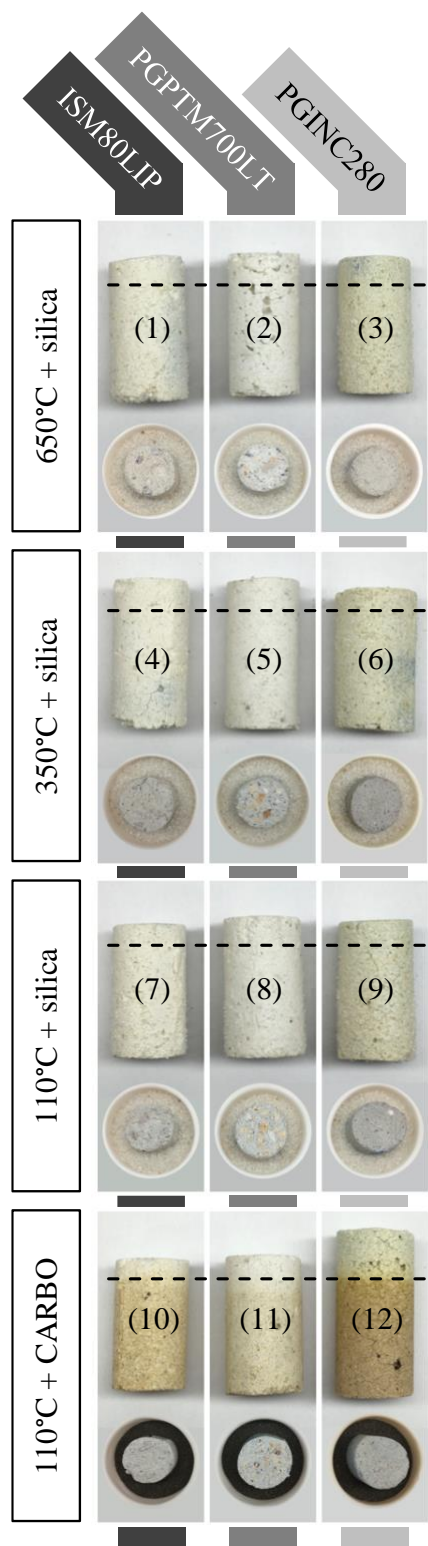


Figure 17. Containment compatibility test images consisting of twelve combinations of partially submerged refractory/media samples before and after 500-hour test in air at 1200°C (dotted lines indicate approximate depth of submersion). Subsequent 500-hour tests were conducted with the same refractory samples in nitrogen and humidified air ( $p_{H_2O}=50\%$ ).

Figure 17 shows the nine candidate hot-face refractory samples partially submersed in Silica 460 prior to testing, as well as the three 110°C refractories in contact with CARBO. Also shown are all twelve refractory/media combinations, labeled numerically, and imaged from the side after the 500-hour (1200°C) test in air. Dotted lines indicate approximate depth of submersion (i.e., the top of the samples were only exposed to furnace atmosphere). Change is observed only for the three refractory/CARBO combinations where it hypothesized that iron has diffused into the refractory.

After each test, samples were removed from particles with relative ease. Only soft agglomeration was observed which disassociated under light mechanical force (e.g., under its own weight). Figure 18 shows the percent change in refractory mass before and after each of the three long-duration (500-hour) tests. The considerable mass loss following the first test in air is due primarily to sample dehydration which should be expected during startup of a commercial operation. This mass loss is understandably more significant for the refractories fired at lower temperature. A small fraction of silica particles stuck to the refractory samples upon removal, most of which could be removed by light mechanical force (e.g., brushing). This fraction of stuck particles is seen to increase slightly for PGINC280 samples following the test in humidified air.

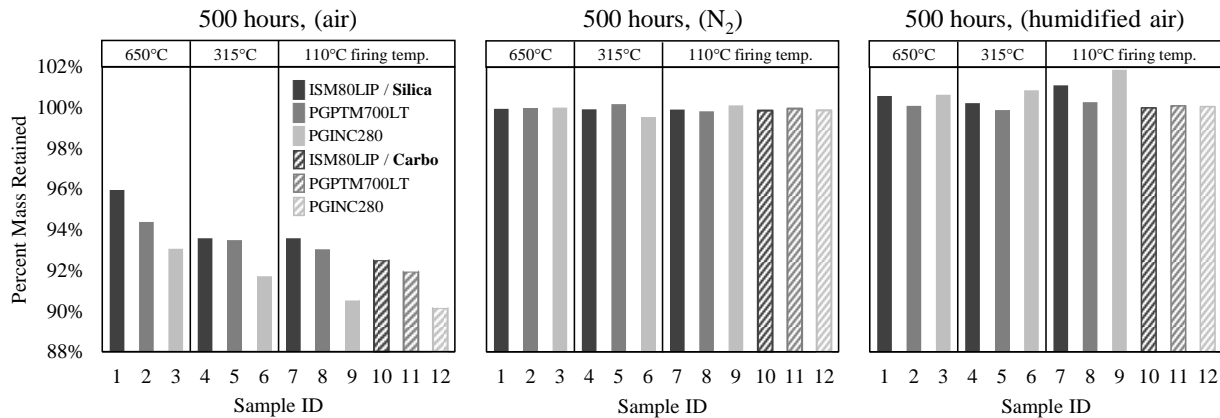


Figure 18. Tracking of mass before and after compatibility tests. Note that the considerable mass loss following the first test in air is attributed primarily to additional sample dehydration relative to the fired temperature.

Following the compatibility test under a compressive ~140 kN load, the silica particles were removed from the crucible with light brushing similar to the non-compressive test. In this case, it is thought that the particles, which are relatively large compared to the inner diameter of the crucible, may have expanded into the softer crucible walls. In practice, this phenomenon is not expected to occur because the particles are not heated in a static setting, but instead, are heated in motion before entering a silo or container.

#### 4. Conclusions

Eight media candidates were identified with potential to support NREL's stand-alone particle-TES system. Using readily available particle information (e.g., cost, thermal stability limit, and composition) and additional key media-specific considerations, a systematic screening process was applied to down-select so that experimental characterization methods could focus on the five most promising candidates.

A total of thirteen particle distributions were sourced with the aim of spanning the Geldart *Group B* particle type for each of the five candidates. High resolution distributions were acquired by Mie scattering, and the relative position of each candidate within the Geldart *Group B* was confirmed. Morphological characterization and optical microscopy for the same five particle types was conducted to determine particle circularity, aspect ratio, solidarity, and convexity: higher circularity indicates that silica and CARBO may outperform CFC and BFA in overall flowability.

For all particle samples, shear cell testing was performed at ambient temperature to characterize each distribution's bulk density, solids fraction, effective angle of internal friction, and angle of internal friction at steady-state flow. An AccuPyc Helium pycnometer was used to determine the real density of each candidate. Although friction angles indicate superior flowability for CARBO products, all candidates demonstrated a "free-flowing" nature. CARBO and BFA benefit from higher real densities, but all BFA and CFC samples exhibit solid fractions on the order of 10% lower than CARBO and silica sands. Future related efforts should include testing at temperature.

Thermal stability screening was performed, revealing an overall increase in soft agglomeration for finer particle samples. Silica sand shows limited soft agglomeration at 1200°C for the two smallest particle distributions. BFA exhibited soft agglomeration at lower temperatures than all other candidates, and both calcined flint clay and SEMCOA demonstrate hard agglomeration at 1000°C. CARBO changed oxidation states and momentarily exhibited soft agglomeration at 1200°C that broke down on the mesh.

Considering results from all characterization methods, CARBO and silica sand appear best-suited to support the stand-alone particle-TES system. Although the physical characteristics of CARBO outperform silica sand in all categories examined, the marginal performance gains are considered insufficient to justify the additional media cost (approximately two magnitudes higher than silica), so silica sand ( $\alpha$ -quartz) is selected as the leading candidate. Future refinement is planned through testing of the pressurized fluidized bed heat-exchanger.

Focused silica sand testing revealed an average heat capacity of 1.1 J/g·°C over the range of 300-1200°C, and a quartz inversion enthalpy of approximately 10.7 J/g. Long-duration and thermal cycling tests are shown to have negligible impacts on particle diameter by volume ( $D_{v50}$ ), and XRD analysis revealed trace crystallographic transitions from  $\alpha$ -quartz and tridymite to  $\beta$ -quartz and  $\alpha$ -cristobalite. Following a 10-hour dwell at 1400°C, only soft agglomeration was observed. Finally, Silica 460 is shown to be compatible with all three Allied Mineral Product refractory candidates, irrespective of firing temperature. Accordingly, further refinement of hot-face selection can be made on the basis of mechanical stability rather than compatibility.

## 5. Acknowledgements

This work was authored in part by the National Renewable Energy Laboratory, operated by Alliance for Sustainable Energy, LLC, for the U.S. Department of Energy (DOE) under Contract No. DE-AC36-08GO28308. Funding provided in part by the DOE Advanced Research Projects Agency–Energy (ARPA-E) DAYS Program under Work Authorization Number 18/CJ000/07/05. The authors thank Dr. Scott Litzelman, Dr. Halle Cheeseman, Dr. Vivien Lecoustre, and Mr. Max Tuttmann for their direction and support. The views expressed in the article do not necessarily represent the views of the DOE or the U.S. Government. The U.S. Government retains and the publisher, by accepting the article for publication, acknowledges that the U.S. Government retains a nonexclusive, paid-up, irrevocable, worldwide license to publish or reproduce the published form of this work, or allow others to do so, for U.S. Government purposes.

## 6. References

- [1] Ma, Z., Glatzmaier, G. C., and Kutscher, C. F., 2012, “The Thermal Energy Storage Solution,” *Solar Today*, **26**(3), pp. 22–26.
- [2] Mehos, M., Turchi, C., Vidal, J., Wagner, M., Ma, Z., Ho, C., Kolb, W., Andraka, C., Ma, Z., Kruiženga, A., and NREL, 2017, *Concentrating Solar Power Gen3 Demonstration Roadmap*.
- [3] NREL, 2018, “Economic Long-Duration Electricity Storage by Using Low-Cost Thermal Energy Storage and High-Efficiency Power Cycle,” News Release [Online]. Available: <https://www.nrel.gov/news/press/2018/nrel-awarded-28m-from-arpa-e-to-develop-low-cost-thermal-energy-storage.html>.
- [4] Babcock & Wilcox, 2021, “Babcock & Wilcox, NREL Sign Exclusive IP Option Agreement for Advanced, Renewable Energy Storage Technology,” News Release [Online]. Available: <https://www.babcock.com/home/about/corporate/news/babcock-wilcox-nrel-sign-exclusive-ip-option-agreement-for-advanced-renewable-energy-storage>.
- [5] Ma, Z., Davenport, P., and Zhang, R., 2020, “Design Analysis of a Particle-Based Thermal Energy Storage System for Concentrating Solar Power or Grid Energy Storage,” *J Energy Storage*, **29**, p. 101382.
- [6] Ma, Z., Wang, X., Davenport, P., Gifford, J., and Martinek, J., 2022, “Preliminary Component Design and Cost Estimation of a Novel Electric-Thermal Energy Storage System Using Solid Particles,” *Journal of Solar Energy Engineering, Transactions of the ASME*, **144**(3).
- [7] Ma, Z., Wang, X., Davenport, P., Gifford, J., Cook, K., Martinek, J., Schirck, J., Morris, A., Lambert, M., and Zhang, R., 2022, “System and Component Development for Long-Duration Energy Storage Using Particle Thermal Energy Storage,” *Appl Therm Eng*, **216**(November 2021), p. 119078.
- [8] Gifford, J., Ma, Z., and Davenport, P., 2020, “Thermal Analysis of Insulation Design for a Thermal Energy Storage Silo Containment for Long-Duration Electricity Storage,” *Front Energy Res*, **8**(June), pp. 1–12.
- [9] Siegel, N. P., Gross, M. D., and Coury, R., 2015, “The Development of Direct Absorption and Storage Media for Falling Particle Solar Central Receivers,” *Journal of Solar Energy Engineering, Transactions of the ASME*, **137**(4), pp. 1–7.
- [10] Albertus, P., Manser, J. S., and Litzelman, S., 2020, “Long-Duration Electricity Storage Applications, Economics, and Technologies,” *Joule*, **4**(1), pp. 21–32.
- [11] O. Ercan Ataer, 2006, “Energy Storage Systems – Storage of Thermal Energy,” *Food Engineering*.

- [12] Siegel, N., Gross, M., Ho, C., Phan, T., and Yuan, J., 2013, “Physical Properties of Solid Particle Thermal Energy Storage Media for Concentrating Solar Power Applications,” *Energy Procedia*, **49**, pp. 1015–1023.
- [13] Baumann, T., and Zunft, S., 2015, “Properties of Granular Materials as Heat Transfer and Storage Medium in CSP Application,” *Solar Energy Materials and Solar Cells*, **143**, pp. 38–47.
- [14] Baeyens, J., and Zhang, H. L., 2017, “High Temperature Concentrated Solar Thermal Power Plant with Particle Receiver and Direct Thermal Storage, Report on Particle Selection for Solar Heat Capture and Storage,” (727762), pp. 1–14.
- [15] Diago, M., Iniesta, A. C., Soum-Glaude, A., and Calvet, N., 2018, “Characterization of Desert Sand to Be Used as a High-Temperature Thermal Energy Storage Medium in Particle Solar Receiver Technology,” *Appl Energy*, **216**(2), pp. 402–413.
- [16] Kang, Q., Flamant, G., Dewil, R., Baeyens, J., Zhang, H. L., and Deng, Y. M., 2019, “Particles in a Circulation Loop for Solar Energy Capture and Storage,” *Particuology*, **43**, pp. 149–156.
- [17] Schroeder, N., and Albrecht, K., 2021, “Assessment of Particle Candidates for Falling Particle Receiver Applications Through Irradiance and Thermal Cycling,” *ASME Energy Sustainability 2021 Conference Proceedings*.
- [18] Geldart, D., 1973, “Types of Gas Fluidization,” *Powder Technol*, **7**, pp. 285–292.
- [19] Leone Young, 2015, “The Coal Ash Opportunity,” *Waste 360* [Online]. Available: <http://www.waste360.com/financials/coal-ash-opportunity>. [Accessed: 21-May-2018].
- [20] Sobczak, J., Purgert, R. M., Doe, C., and Number, G., 2002, “The Use of Fly Ash as an Aggregate for Foundry Sand Mold and Core Production,” *Energy*, pp. 1–56.
- [21] Ghaly, A. E., and Ergudenler, A., 1993, “Agglomeration of Silica Sand in a Fluidized Bed Gasifier Operating on Wheat Straw,” *Agricultural Engineering*, **4**(2), pp. 135–147.
- [22] Chaivatamaset, P., Sricharoon, P., Tia, S., and Bilitewski, B., 2014, “The Characteristics of Bed Agglomeration/Defluidization in Fluidized Bed Firing Palm Fruit Bunch and Rice Straw,” *Appl Therm Eng*, **70**(1), pp. 737–747.
- [23] Chaivatamaset, P., and Tia, S., 2015, “The Characteristics of Bed Agglomeration during Fluidized Bed Combustion of Eucalyptus Bark,” *Appl Therm Eng*, **75**, pp. 1134–1146.
- [24] Deer, W. A., Howie, R. A., and Zussman, J., 2013, *An Introduction to the Rock-Forming Minerals*, Mineralogical Society of Great Britain and Ireland.
- [25] Davenport, P., Ma, Z., Nation, W., Schirck, J., and Lambert, M., “Thermal Stability of Silica for Application in Thermal Energy Storage,” *SolarPACES 2020 Conference Proceedings*, (in press).
- [26] Park, C., and Charlemagne, B., 2009, “Kaolin Calcined , Mullite and Clays , Flint , Calcined Joint Pre-SIEF Meeting,” (465221502).
- [27] Hurlbut, C.S., Cornelis, K., 1985, *Manual of Mineralogy*, Wiley.
- [28] Knott, R. C., Sadowski, D. L., Jeter, S. M., Abdel-Khalik, S. I., Al-Ansary, H. A., and El-Leathy, A., 2014, “Sintering of Solid Particulates under Elevated Temperature and Pressure in Large Storage Bins for Thermal Energy Storage,” *ASME 2014 8th International Conference on Energy Sustainability, ES 2014 Collocated with the ASME 2014 12th International Conference on Fuel Cell Science, Engineering and Technology*, **1**, pp. 1–6.
- [29] Jenike, A. W., 1964, “Storage and Flow of Solids,” *Bulletin No. 123, University of Utah*, **53**.

- [30] Chase, M.W., Jr., 1998, "NIST-JANAF Thermochemical Tables," J. Phys. Chem. Ref. Data, Monograph 9, **4**, pp. 1-1951 (<https://webbook.nist.gov/cgi/cbook.cgi?ID=>.
- [31] Damby, D. E., Llewellyn, E. W., Horwell, C. J., Williamson, B. J., Najorka, J., Cressey, G., and Carpenter, M., 2014, "The  $\alpha$ - $\beta$  Phase Transition in Volcanic Cristobalite," J Appl Crystallogr, **47**(4), pp. 1205–1215.
- [32] Ghiorso, M. S., Carmichael, I. S. E., and Moret, L. K., 1979, "Inverted High-Temperature Quartz: Unit Cell Parameters and Properties of the  $\alpha$ - $\beta$  Inversion," Contributions to Mineralogy and Petrology, **68**(3), pp. 307–323.
- [33] Kingery, W. D., Bowen, H. K., and Uhlmann, D. R., 1976, *Introduction to Ceramics*.